Geophysical Research Letters

RESEARCH LETTER
10.1029/2019GL085400

First Synoptic Observations of Geomagnetic Storm Effects on the Global-Scale OI 135.6-nm Dayglow in the Thermosphere by the GOLD Mission

Quan Gan[1], Richard W. Eastes[1], Alan G. Burns[2], Wenbin Wang[2], Liying Qian[2], Stanley C. Solomon[2], Mihail V. Codrescu[3], Joseph McInerney[2], and William E. McClintock[1]

[1]Laboratory for Atmospheric and Space Physics, University of Colorado Boulder, Boulder, CO, USA, [2]High Altitude Observatory, National Center for Atmospheric Research, Boulder, CO, USA, [3]Space Weather Prediction Center, National Oceanic and Atmospheric Administration, Boulder, CO, USA

Key Points:
- GOLD provided, for the first time, synoptic observations of the thermospheric response to a geomagnetic storm with a 30-min cadence
- Dayglow brightness depletions occurred at high latitudes and were extended into midlatitudes with evident interhemispheric asymmetry
- The deepest depletion occurred near local noon and moved westward during and after the geomagnetic storm

Supporting Information:
- Movie S1
- Figure S1

Correspondence to:
Q. Gan,
blondganquan@gmail.com

Citation:
Gan, Q., Eastes, R. W., Burns, A. G., Wang, W., Qian, L., Solomon, S. C., et al. (2020). First synoptic observations of geomagnetic storm effects on the global-scale OI 135.6-nm dayglow in the thermosphere by the GOLD mission. *Geophysical Research Letters*, *47*, e2019GL085400. https://doi.org/10.1029/2019GL085400

Received 13 SEP 2019
Accepted 10 JAN 2020
Accepted article online 21 JAN 2020

The copyright line for this article was changed on 29 MAY 2020 after original online publication.

Abstract The Global-scale Observations of the Limb and Disk (GOLD) mission provides, for the first time, a synoptic view of the thermospheric response to a moderate geomagnetic storm at a 30-min cadence. The observations showed that the OI 135.6-nm emission substantially decreased at middle and high latitudes, but it increased at low latitudes. The depletion pattern between 4 and 6 November 2018 was likely due to the strong upwelling of the high-latitude thermosphere. The deepest depletion in brightness that occurred near local noon was of ~300–400 R (~35% of the quiet time background level) and displayed a striking westward movement. First-principles modeling reasonably reproduced the overall morphology of brightness response to the geomagnetic storm despite the depletion magnitude in brightness being underestimated. The postprocessing of the simulation results revealed that the westward movement of the deepest depletion was attributable to the horizontal wind changes driven by the geomagnetic storm.

Plain Language Summary Geomagnetic storms are triggered by enhanced solar wind emitted from the Sun, and a large portion of the absorbed solar energy dissipates into the high latitudes of the Earth's atmosphere through Joule heating and ion drag. Geomagnetic storms usually bring tremendous disturbances into the thermosphere-ionosphere (e.g., neutral and plasma density), which significantly impact human activities (e.g., satellite orbit determination, navigation, and telecommunications). Accurate prediction of the response to geomagnetic storms in the thermosphere-ionosphere is one of the core scientific objectives of space weather. The newly launched Global-scale Observations of the Limb and Disk mission provides unprecedented synoptic measurements of ionosphere-thermosphere properties. This study reports a large response of the OI 135.6-nm emission to a moderate geomagnetic storm that occurred on 8–9 November 2018 observed by Global-scale Observations of the Limb and Disk, which demonstrates a huge potential to advance our knowledge of the thermosphere-ionosphere system and ability to simulate and forecast space weather.

1. Introduction

The Earth's thermosphere is an externally driven system that accommodates complex processes of energy and momentum deposition, dissipation, and conversion. Neutral density and composition are of particular interest and importance since they affect the orbits of satellites, space debris, and plasma densities in the Earth's ionosphere (Burns et al., 2013; Crowley, 1991; Forbes, 2007; Roble, 1983; Sarris, 2019). The sources of significant thermospheric changes in neutral density and composition include geomagnetic storms and solar radiation from above (Prolss, 2011) and atmospheric waves of various scales from below (Akmaev, 2011; Liu, 2016; Oberheide et al., 2015; Vincent, 2015). Geomagnetic storms cause large changes in thermospheric densities at high latitudes via Joule heating, and the changes are then extended into the middle and low latitudes via the resulting changes in global circulation (Burns et al., 2007; Prolss, 2011; Richmond & Lu, 2000). The pioneering studies on this subject date back to Allan (1972) and references therein. Over the past two decades, considerable advances have been made in understanding the effects of geomagnetic storms on the global thermosphere by instruments in low-Earth orbit (LEO) (Bruinsma et al., 2006; Burns

& Killeen, 1992; Forbes et al., 1996; Lei et al., 2008; Liu & Luhr, 2005; Sutton et al., 2005) and by general circulation models (Burns et al., 1995, 1991; Fujiwara et al., 1996; Fuller-rowell et al., 1994; Fuller-Rowell et al., 1996).

However, previous observational studies, especially those based on polar-orbiting LEO satellites, were incapable of separating temporospatial changes and providing a synoptic, global-scale view of geomagnetic storm effects. This is because, for instance, LEO satellites usually sample in an asynoptic way. On the other hand, synoptic measurements, which mean simultaneous global-scale measurements at uniform increments in time, can be achieved from the geostationary orbit.

In addition, thermospheric observations remain rather rare. The routine thermosphere monitoring we have is made by either ground-based instruments with limited spatial coverage at high temporal resolution or LEO satellite-based instruments with global-scale coverage at limited temporal resolution. Having continuous and global-scale observations at high time cadence enables advances in understanding of the physical processes that change the thermosphere-ionosphere and improvements in the ability of general circulation models to simulate the changes. With this objective, the National Aeronautics and Space Administration GOLD (Global-scale Observations of the Limb and Disk) mission successfully launched a far ultraviolet (FUV) imager into the geostationary orbit on 25 January 2018. The imager is a hosted payload on the SES-14 satellite. The FUV imager has two channels; each has a plane scan mirror capable of scanning the entire disk of the Earth. The GOLD mission data products include daytime brightness of the FUV emissions, neutral temperatures, O/N_2 column density ratios, and the nighttime peak electron densities on the disk. In this study, we use disk dayglow emission measurements to describe the storm time behavior of thermospheric composition in a synoptic way for the first time. The readers are referred to Eastes et al. (2017) for the details of mission objectives, instrument, and data products. Most recently, the nighttime disk scans have been used to depict the morphology of the equatorial ionization anomaly (see Eastes et al., 2019).

This study presents the first observational evidence of the large OI 135.6-nm emission changes that occurred on the Days 309–310 in 2018 as a consequence of a geomagnetic storm. Brightness change is proportional to the change in atomic oxygen mass mixing ratio and is a proxy for the composition response to geomagnetic storms. As it is shown in Figure 1, Kp (top panel) was 5 at 1800–2400 UT on Day 308 (4 November 2018) and reached 6 at 0300–0600 UT on Day 309. The Dst index (middle panel) shows that the main phase of the geomagnetic storm occurred around 1000 UT of Day 308. The strong energy and momentum inputs due to the substorms primarily occurred between 1500 UT on Day 308 and 1400 UT on Day 309 as the AL index (bottom panel) demonstrated sharp jumps, consistent with Kp, which was greater than 4. In the OI 135.6-nm emissions, GOLD observed a substantial depletion at middle and high latitudes relative to the quiet time level. First-principles model calculation reproduced the general morphology of the geomagnetic storm effect on the brightness, but it underestimated the magnitude of the brightness depletions and overestimated their latitudinal extent. The paper is organized as follows. Section 2 overviews the GOLD data and the models used in this study. Section 3 presents the major findings. Section 4 gives the conclusions.

2. Data and Model

In this study, we use the atomic oxygen emission at 135.6 nm from GOLD L1C disk images measured by Channel A, which has the most extensive dayside coverage. During a scan, the 10.8° tall image of the spectrometer entrance slit crosses the disk in two swaths; one covers the northern latitudes and the other covers the southern latitudes. All disk scans are performed east to west. The L1C disk images are binned at a constant angular resolution that is equivalent to approximately 125 km × 125 km at nadir. The atomic oxygen 135.6-nm emission was integrated from 133 to 137 nm. Note that the 135.6-nm brightness persists at night due to photon production by recombination of the ionosphere. The entrance slits of each channel can provide spectral resolution of 0.21 nm or 0.35 nm, depending on the mission objectives. The former was employed during the geomagnetic storm observation we discussed here. While a band of the N_2 Lyman-Birge-Hopfield (LBH) emission (3,0 at 135.4 nm) overlaps the OI 135.6-nm peak, the contribution is small. Based on the LBH bands at ~138.4 nm (5,2 and 2,0), the relative vibrational populations observed by GOLD and laboratory data (Franck-Condon factors of

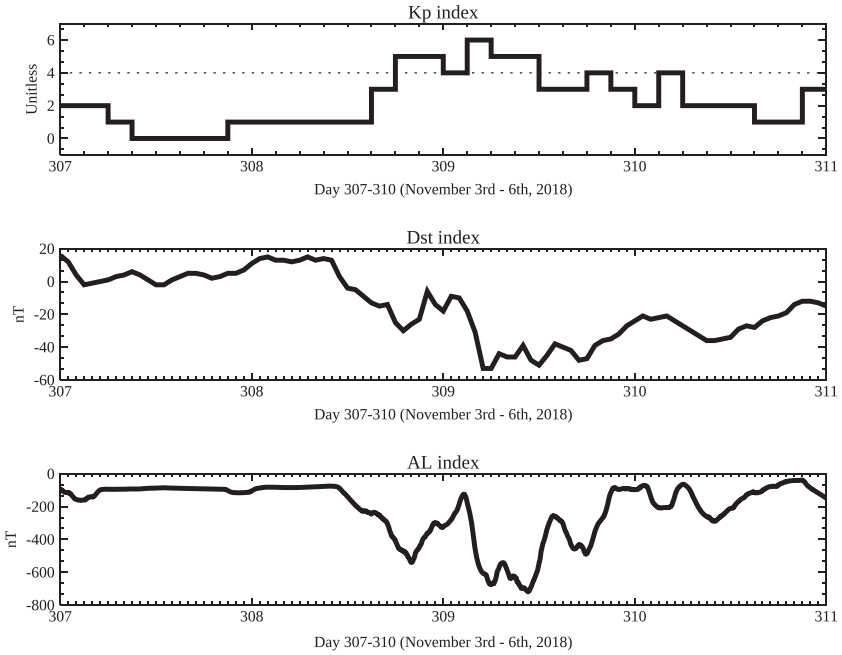

Figure 1. The 3-hourly Kp (top panel), hourly Dst and AL indices (middle and bottom panels) on Days 307–310 (3–6 November) in 2018. The dotted line marks the value of 4 in Kp.

Benesch et al., 1966), the N_2 LBH contribution to the emission observed at ~135.6 nm is only 9–12% of the total. The L1C data and documentation guide are available online (http://gold.cs.ucf.edu).

The neutral atmosphere is simulated by the TIE-GCM (Thermosphere Ionosphere Electrodynamics General Circulation Model), a first-principles general circulation model developed at National Center of Atmospheric Research. It simulates the circulation, temperature, compositions, and electrodynamics by self-consistently solving the fully coupled hydrodynamics, thermodynamics, and mass continuity equations of the neutral atmosphere along with ion energy, ion momentum, and ion continuity equations from the mesopause (~100 km) through the thermosphere (Roble et al., 1988). A recent description of the model is given by Qian et al. (2014). Lower atmospheric diurnal and semidiurnal tides are prescribed by the global-scale wave model (Hagan et al., 1999) at the model lower boundary. Low-latitude ionospheric dynamo electric fields are self-consistently calculated in the TIE-GCM using the modeled ionospheric conductivity and neutral winds (Richmond et al., 1992). Magnetospheric forcing is driven by the Heelis et al. (1982) model that gives an empirical specification of electric potential parameterized by the geomagnetic Kp index. The auroral precipitation is specified using the formulation described by Roble and Ridley (1987), which is also parameterized by the Kp index. The solar $F10.7$ cm index is used as a proxy of the solar extreme ultraviolet radiation over the Days 305–311 (1–7 November) in 2018. The model is run at a horizontal resolution of 2.5° (latitude) × 2.5° (longitude).

The neutral atmosphere and ionosphere from the TIE-GCM are then used by the GLOW (Global airgLOW) model to calculate the OI 135.6-nm emission. GLOW is a single-column, single-time model that is run repeatedly to generate global maps that are coincident in time with the GOLD images. It computes ionization, dissociation, and excitation rates; performs energetic electron transport calculations; applies ion-neutral chemistry; and outputs the airglow emission rates. The readers are referred to Solomon (2017) for details.

3. Results and Discussion

Figure 2 displays the GOLD observations of OI 135.6-nm emission brightness at five universal times on Day 307 (3 November 2018) as well as the brightness changes over the following Days 308–310 (4–6 November 2018). Brightness changes were calculated by subtracting the brightness of the geomagnetically Quiet Day

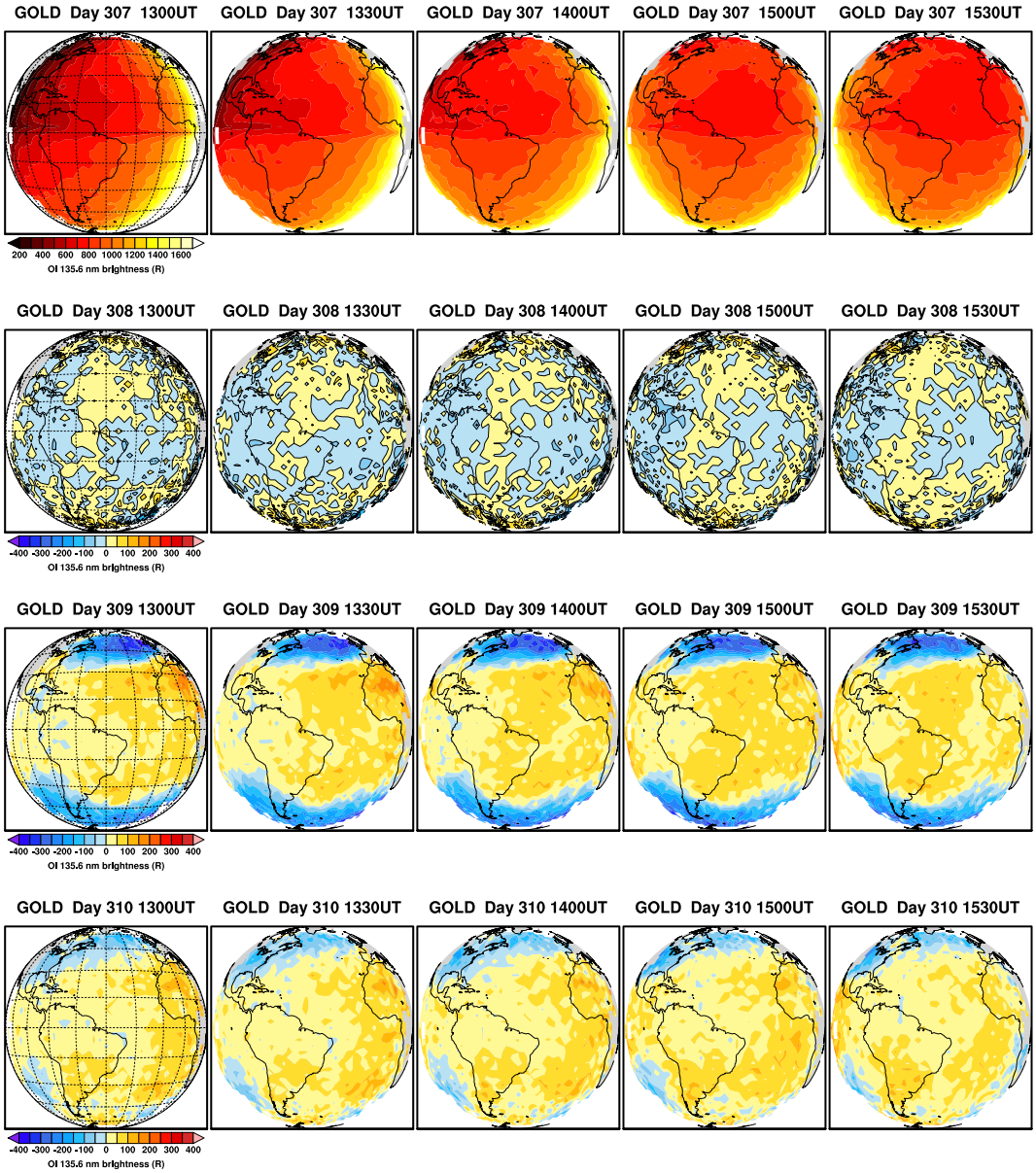

Figure 2. GOLD images of the OI 135.6-nm airglow brightness at 1300, 1330, 1400, 1500, and 1530 UT (from left to right) on Days 307–310 (from top to bottom), 2018. The GOLD maps on Days 308–310 are the differences from that on Day 307. The GOLD images on Day 307 are the original disk scans. The brightness value interval is 50 R. The interval of the geographic grids (dotted line) is 15° on either longitude or latitude. The center of the map is located at 45°W and the equator.

307 from that of Days 308–310 at the same universal times. Under geomagnetically quiet conditions (first row, Day 307), the brightness was on the order of 200–1600 Rayleigh (R) depending on the solar zenith angle. Specifically, the brightness (top left panel, 1300 UT) was ~1100 R at local noon and decreased to ~200 R near dawn. At 1500 UT (fourth panel on the first row), the brightness pattern was almost symmetric about 45°W longitude since the local time of the subsatellite point was near local noon. A slightly higher brightness occurred in the Southern Hemisphere (SH) due to the smaller solar zenith angles. Note that the brightness on the edge of the disk could be the greatest due to the large emission angle, but this was not an issue in quantifying the storm-induced changes that were calculated on each individual universal time between different days, as brightness distribution due to either solar zenith angle or emission angle is not changed significantly over short periods. On Day 308 (second row, 4

November 2018), which was geomagnetically quiet before 1800 UT, the brightness relative to that of Day 307 appeared as a patch of enhancement over the Atlantic. Since the pattern is persistent and the brightness is greater than the random noise (~25 R), it may indicate a possible connection to the large-scale waves from below (Chang et al., 2010; Forbes et al., 2018; Gan et al., 2015, 2017; Oberheide et al., 2009; Yue & Wang, 2014). A possible pathway through which atmospheric waves produce signatures in composition was suggested by Ward (1999). A detailed study is needed to establish this connection.

We now turn to the Geomagnetic Storm Day 309 (third row, 5 November 2018). The observations showed great changes in the OI 135.6-nm emission on the disk. Specifically, the depletion attained ~350 R poleward of 30°N in the Northern Hemisphere (NH), equivalent to ~35% of the quiet time background level. The SH middle and high latitudes showed a somewhat weaker depletion of ~250 R. A boundary between low-latitude enhancements and higher-latitude depletions was situated at ~20–40° (the geographic grid interval was 15° as marked in the left column, and the map was centered at 45°W over the equator) depending on longitudes in both hemispheres. For instance, the boundary in the SH moved to ~20°S in the 75–90°W longitude sector, whereas the boundary was poleward of 30°S at other longitudes. Interestingly, the boundary in the NH at ~90°W extended to a higher latitude of ~45°N forming a mesoscale "hook" structure in all the images on Day 309. We postulate that such a localized feature might be related to the thermospheric dynamics including the Joule heating and horizontal wind divergence/convergence. This feature will be further explored in a separate paper. On Day 310 (fourth row, 6 November 2018), the geomagnetic storm effect was fading away; however, a ~150 R brightness depletion can still be seen at middle and high latitudes of both hemispheres in the geomagnetic storm recovery phase. Previous studies suggested that the depletion of atomic oxygen at middle and high latitudes during a geomagnetic storm is mainly attributable to the strong upwelling as a result of enhanced Joule heating and ion drag. The low-latitude enhancement of atomic oxygen could be caused by the resulting equatorward and downward circulation (Burns et al., 1995). Overall, the GOLD observations delineated an asymmetry of the storm-induced brightness depletion and thereby atomic oxygen mass mixing ratio reduction between the two hemispheres. Namely, the higher-latitude depletion of OI 135.6-nm emission brightness in the NH was greater than in the SH, whereas the latter covered a more extensive region in the GOLD field of view. Several mechanisms have been proposed to account for such interhemispheric asymmetry in the literature. For instance, there is an asymmetry in the energy input of Joule heating and momentum inputs of ion drag in the GOLD field of view due to the geographic asymmetry of the magnetic poles. Then, the storm-induced circulation is hemisphere dependent, and the resulting boundary between low-latitude enhancement and higher-latitude depletion could be morphologically different. Meanwhile, the prevailing summer-to-winter circulation in the thermosphere (from the SH to the NH in this case) due to the solar extreme ultraviolet heating also affects the extent of the middle- and high-latitude depletion region (Fuller-Rowell et al., 1996; Prolss & Zahn, 1977 Qian et al., 2016). Furthermore, the B_y polarity (y component of the interplanetary magnetic field) is another possible candidate to explain the magnitude and the spatial extent of depletions (Goncharenko et al., 2006; Immel et al., 1997). We would like to point out that the significant geomagnetic storm effect in brightness has been observed since the first disk scan on 0630 LT of Day 309 (see supporting information Movie S1 that shows the evolution of brightness changes on a 30-min basis from Day 308 to 310). On Day 310 when the Kp index was less than 4 (recovering phase as indicated by Dst in Figure 1), storm-driven brightness depletions still existed in the GOLD images, despite these depletions in middle and high latitudes being considerably weakened.

Figure 3 illustrates a comparison of the brightness changes between GOLD observations and TIE-GCM+GLOW calculations. We selected three GOLD images for a detailed comparison, including the pre-storm onset (left column) and storm-driven (right two columns) moments. All the UTs given are near local noon at the subsatellite point (less than 3-hr difference). This ensures that dayglow observations are available on the whole disk. Also, the contour level is reduced to 25 R to aid quantitative comparison of fine structures. At 1600 UT on Day 308 (left column), which was just before the storm onset, GOLD (upper left panel) observed the patches of ~50 R brighter emission in both hemispheres, approximately symmetric with respect to the equator. Even though it was weak, the brightness was enhanced over an extensive area, unambiguously indicating a small enhancement of atomic oxygen densities. The model (bottom left panel) does not, however, reproduce a coincident signature.

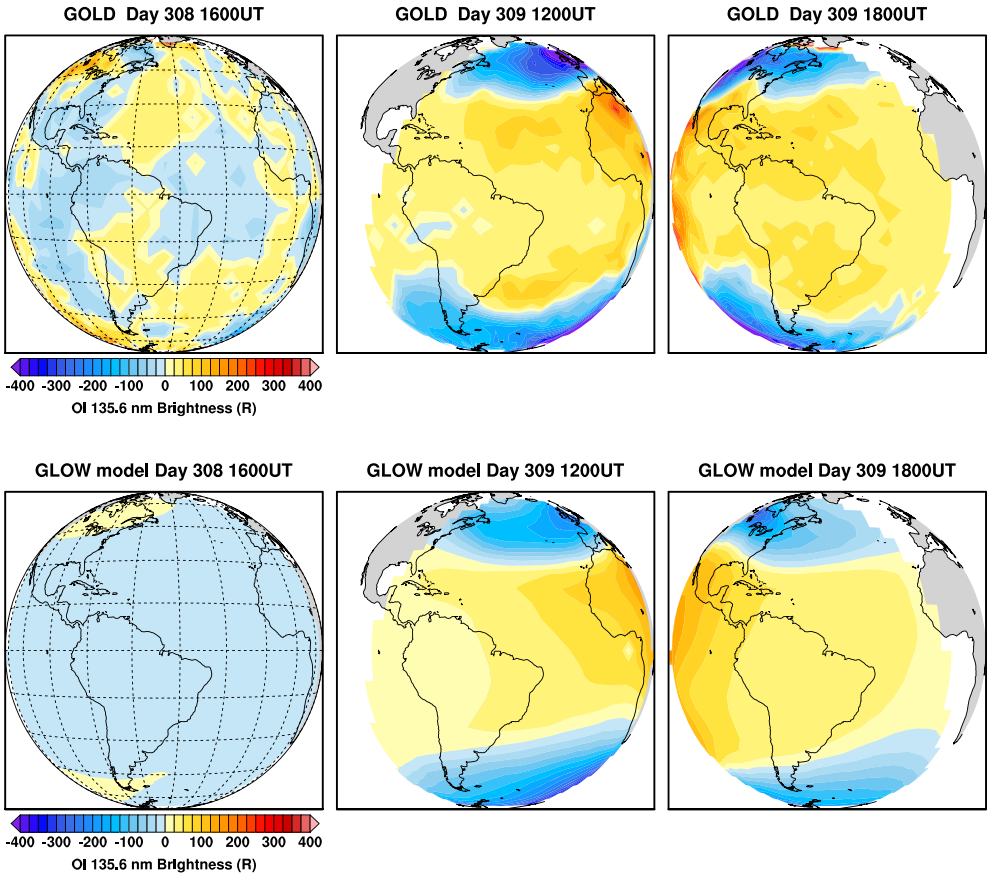

Figure 3. A comparison of the OI 135.6-nm brightness change between the observations and the simulations at 1600 UT on Day 308 (left, Kp = 3), and at 1200 UT (middle, Kp = 5), 1800 UT (right, Kp = 3) on Day 309. The brightness value interval is 25 R. The interval of the geographic grids (dotted line) is 15° on either longitude or latitude. The center of the map is located at 45°W and the equator.

At 1200 UT on Day 309, when the geomagnetic storm effect was dominant, the simulation (bottom middle panel) compares well with the GOLD observation (top middle panel), in particular regarding to the depletion of OI 135.6-nm emission at higher latitudes. Both the observations and the simulations exhibited the greatest brightness change (either depletion or enhancement) near local noon at those UTs, and the brightness change tended to be smaller toward the early morning sector. However, we note some discrepancies between data and model. First, the maximum depletion in middle and high latitudes was underestimated by ~100–150 R by the model. The difference of the overall shape of the depletion region was evident between the observation and the simulation in the SH. The observed depletion region was extended toward the equator near the west coast of the South America, but it was not reproduced by the TIE-GCM. The possible reasons include, but are not limited to, that the empirical high-latitude inputs of convection pattern and auroral precipitation in the TIE-GCM may differ from the actual energy and momentum inputs, and the model thus would not accurately simulate the strength and shape of the depletions. A similar scenario is found when comparing data and model at 1800 UT of Day 309 (right column). Merging the results (on Day 309) in Figure 2, it is seen that the region of deepest depletion, especially in the NH, appeared to move westward between 1200 and 1800 UT. This phenomenon was qualitatively reproduced by the TIE-GCM+GLOW (see supporting information Figure S2). It thus merits a closer look at the simulation results to elaborate on the driver of this behavior. As it is seen in Figure 4, the atomic oxygen showed the deepest depletion in the region of 10–30°W and 55–65°N at 0600 UT on Day 309, and the deepest depletion moved westward with time (note that the region poleward of 70°N is not covered by the GOLD's field of view). The simulated horizontal winds were strongly southward at 0600 UT but turned westward in the following hours. A possible scenario is that Joule heating

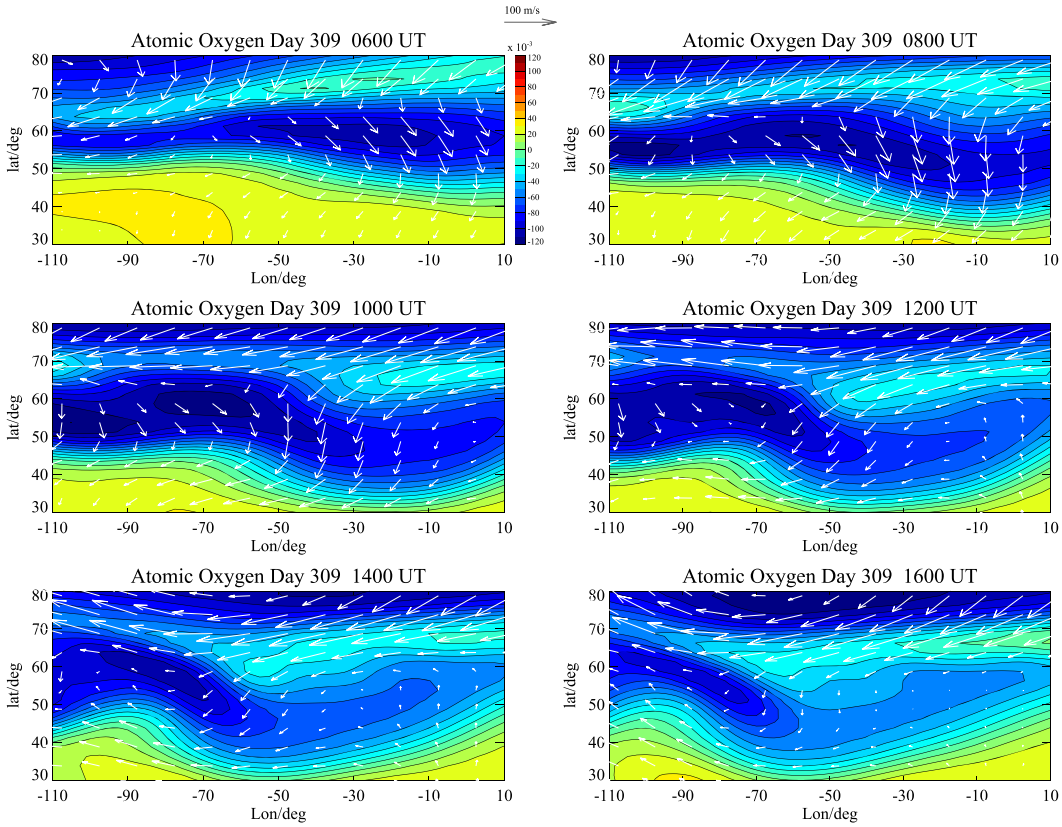

Figure 4. Atomic oxygen (in mmr) and horizontal winds (in m/s, vectors) as functions of latitude and longitude on Day 309 relative to those on Day 307 between 0600 and 1600 UT at a 2-hr cadence. The results shown here are at level = −2 in the TIE-GCM (approximately 160 km).

produced temperature enhancement, which set up a pressure gradient force driving equatorward winds at 0600 UT in the region where the deepest depletion occurred. Subsequently, the equatorward wind turned westward due to the balance between the Coriolis force and the pressure gradient force. Considering the high correlation between the strengthened westward winds and the atomic oxygen depletions in the same region, we thus suggest that the horizontal winds, advecting the air parcels, played a major role in the westward motion of the greatest depletion area. This indicates a strong dynamical control of the storm time thermospheric composition variability.

4. Conclusions

In this study, we describe the National Aeronautics and Space Administration GOLD observations of the thermospheric response to a moderate geomagnetic storm occurring on Days 309–310, 2018. This is the first time that a global-scale synoptic view of thermospheric evolution during a geomagnetic storm is achieved at this high 30-min cadence. The GOLD images demonstrated substantial depletions of ~35% (300–400 R) in OI 135.6-nm emission relative to the quiet time background level at middle and high latitudes of both hemispheres. The shape of the depletion region displayed asymmetry between the NH and the SH. The deepest depletion tended to occur near local noon and displayed a westward motion. The first-principles modeling (TIE-GCM+GLOW) reproduced the overall morphology of the OI 135.6-nm emission response to the geomagnetic storm, but the model calculation underestimated the depletion strength by up to 40–50%. A further analysis of the simulation results revealed that the westward horizontal winds were the crucial driver of the westward motion of the depletion area in atomic oxygen. GOLD is providing new information of thermosphere-ionosphere dynamics with unprecedented, synoptic observations of daytime airglow emission, and a good opportunity to advance our capability to forecast space weather.

Acknowledgments

We wish to thank Janet Kozyra for the discussion on the geomagnetic storm indices used in the study. Q. G. and R. E. are supported by NASA Contract 80GSFC18C006. W. W. is supported by NASA Grants NNX14AE06G, NNX15AB83G, NNX16AH06G, NNX17AI42G, 80NSSC17K0013, and 80NSSC19K0278. L. Q. is supported by NASA Grants NNX16AH06G and 80NSSC19K0278. NCAR is sponsored by the National Science Foundation. The Level 1C data used in this study are available at the GOLD Science Data Center (http://gold.cs.ucf.edu/search/) and at NASA's Space Physics Data Facility (http://spdf.gsfc.nasa.gov). The GLOW model simulation data are available online (https://1drv.ms/u/s!An2zQdOzk5phjdJbTJlBM6BYMa8jYw?e=LCJU37).

References

Akmaev, R. A. (2011). Whole atmosphere modeling: Connecting terrestrial and space weather. *Reviews of Geophysics*, *49*, RG4004. https://doi.org/10.1029/2011RG000364

Allan, R. R. (1972). Upper-atmosphere heating near auroral zones. *Nature*, *235*(5333), 100–102. https://doi.org/10.1038/235100a0

Benesch, W., Vanderslice, J. T., Tilford, S. G., & Wilkinson, P. G. (1966). Franck-Condon factors for observed transitions in N2 above 6 eV. *Astrophysical Journal*, *143*, 236–252. https://doi.org/10.1086/148494

Bruinsma, S., Forbes, J. M., Nerem, R. S., & Zhang, X. (2006). Thermosphere density response to the 20–21 November 2003 solar and geomagnetic storm from CHAMP and GRACE accelerometer data. *Journal of Geophysical Research*, *111*, A06303. https://doi.org/10.1029/2005JA011284

Burns, A. G., & Killeen, T. L. (1992). The equatorial neutral thermospheric response to geomagnetic. *Geophysical Research Letters*, *19*(10), 977–980. https://doi.org/10.1029/92gl00522

Burns, A. G., Killeen, T. L., Carignan, G. R., & Roble, R. G. (1995). Large enhancements in the O/N_2 ratio in the evening sector of the winter hemisphere during geomagnetic storms. *Journal of Geophysical Research*, *100*(A8), 14,661–14,671. https://doi.org/10.1029/94JA03235

Burns, A. G., Killeen, T. L., & Roble, R. G. (1991). A theoretical-study of thermospheric composition perturbations during an impulsive geomagnetic storm. *Journal of Geophysical Research*, *96*(A8), 14,153–14,167. https://doi.org/10.1029/91JA00678

Burns, A. G., Solomon, S. C., Wang, W., & Killeen, T. L. (2007). The ionospheric and thermospheric response to CMEs: Challenges and successes. *Journal of Atmospheric and Solar-Terrestrial Physics*, *69*(1-2), 77–85. https://doi.org/10.1016/j.jastp.2006.06.010

Burns, A. G., Wang, W., Solomon, S. C., & Qian, L. (2013). Energetics and Composition in the Thermosphere. In J. Huba, R. Schunk, & G. Khazanov (Eds.), *Modeling the Ionosphere-Thermosphere System* (Vol. 201, pp. 39–48). Washington: American Geophysical Union. https://doi.org/10.1029/2012gm001292

Chang, L. C., Palo, S. E., Liu, H. L., Fang, T. W., & Lin, C. S. (2010). Response of the thermosphere and ionosphere to an ultra fast Kelvin wave. *Journal of Geophysical Research*, *115*, A00G40. https://doi.org/10.1029/2010JA015453

Crowley, G. (1991). Dynamics of the Earths thermosphere—A review. *Reviews of Geophysics*, *29*, 1143–1165. https://doi.org/10.1002/rog.1991.29.s2.1143

Eastes, R. W., McClintock, W. E., Burns, A. G., Anderson, D. N., Andersson, L., Codrescu, M., et al. (2017). The Global-Scale Observations of the Limb and Disk (GOLD) mission. *Space Science Reviews*, *212*(1-2), 383–408. https://doi.org/10.1007/s11214-017-0392-2

Eastes, R. W., Solomon, S. C., Daniell, R. E., Anderson, D. N., Burns, A. G., England, S. L., et al. (2019). Global-scale observations of the equatorial ionization anomaly. *Geophysical Research Letters*, *46*, 9318–9326. https://doi.org/10.1029/2019GL084199

Forbes, J. M. (2007). Dynamics of the thermosphere. *Journal of the Meteorological Society of Japan*, *85B*, 193–213. https://doi.org/10.2151/jmsj.85B.193

Forbes, J. M., Gonzalez, R., Marcos, F. A., Revelle, D., & Parish, H. (1996). Magnetic storm response of lower thermosphere density. *Journal of Geophysical Research*, *101*(A2), 2313–2319. https://doi.org/10.1029/95ja02721

Forbes, J. M., Zhang, X., Maute, A., & Hagan, M. E. (2018). Zonally symmetric oscillaitons of the thermosphere at planetary wave periods. *Journal of Geophysical Research, Space Physics*, *123*(5), 4110–4128. https://doi.org/10.1002/2018JA025258

Fujiwara, H., Maeda, S., Fukunishi, H., Fuller-Rowell, T. J., & Evans, D. S. (1996). Global variations of thermospheric winds and temperatures caused by substorm energy injection. *Journal of Geophysical Research*, *101*(A1), 225–239. https://doi.org/10.1029/95JA01157

Fuller-rowell, T. J., Codrescu, M. V., Moffett, R. J., & Quegan, S. (1994). Response of the thermosphere and ionosphere to geomagnetic storms. *Journal of Geophysical Research*, *99*(A3), 3893–3914. https://doi.org/10.1029/93JA02015

Fuller-Rowell, T. J., Codrescu, M. V., Rishbeth, H., Moffett, R. J., & Quegan, S. (1996). On the seasonal response of the thermosphere and ionosphere to geomagnetic storms. *Journal of Geophysical Research*, *101*(A2), 2343–2353. https://doi.org/10.1029/95JA01614

Gan, Q., Oberheide, J., Yue, J., & Wang, W. B. (2017). Short-term variability in the ionosphere due to the nonlinear interaction between the 6-day wave and migrating tides. *Journal of Geophysical Research, Space Physics*, *122*(8), 8831–8846. https://doi.org/10.1002/2017JA023947

Gan, Q., Yue, J., Chang, L. C., Wang, W. B., Zhang, S. D., & Du, J. (2015). Observations of thermosphere and ionosphere changes due to the dissipative 6.5-day wave in the lower thermosphere. *Annales Geophysicae*, *33*(7), 913–922. https://doi.org/10.5194/angeo-33-913-2015

Goncharenko, L., Salah, J., Crowley, G., Paxton, L. J., Zhang, Y., Coster, A., et al. (2006). Large variations in the thermosphere and ionosphere during minor geomagnetic disturbances in April 2002 and their association with IMF *By*. *Journal of Geophysical Research*, *111*, A03303. https://doi.org/10.1029/2004JA010683

Hagan, M. E., Burrage, M. D., Forbes, J. M., Hackney, J., Randel, W. J., & Zhang, X. (1999). GSWM-98: Results for migrating solar tides. *Journal of Geophysical Research*, *104*(A4), 6813–6827.

Heelis, R. A., Lowell, J. K., & Spiro, R. W. (1982). A model of the highlatitude ionosphere convection pattern. *Journal of Geophysical Research*, *87*, 6339. https://doi.org/10.1029/JA087iA08p06339

Immel, T. J., Craven, J. D., & Frank, L. A. (1997). Influence of IMF *By* on large-scale decreases of O column density at middle latitudes. *Journal of Atmospheric and Solar-Terrestrial Physics*, *59*(6), 725–737. https://doi.org/10.1016/s1364-6826(96)00099-5

Lei, J., Wang, W., Burns, A. G., Solomon, S. C., Richmond, A. D., Wiltberger, M., et al. (2008). Observations and simulations of the ionospheric and thermospheric response to the December 2006 geomagnetic storm: Initial phase. *Journal of Geophysical Research*, *113*, A01314. https://doi.org/10.1029/2007JA012807

Liu (2016). Variability and predictability of the space environment as related to lower atmosphere forcing. *Space Weather*, *14*(9), 634–658. https://doi.org/10.1002/2016SW001450

Liu, H., & Luhr, H. (2005). Strong disturbance of the upper thermospheric density due to magnetic storms: CHAMP observations. *Journal of Geophysical Research*, *110*, A09S29. https://doi.org/10.1029/2004JA010908

Oberheide, J., Forbes, J. M., Hausler, K., Wu, Q., & Bruinsma, S. L. (2009). Tropospheric tides from 80 to 400 km: Propagation, interannual variability, and solar cycle effects. *Journal of Geophysical Research*, *114*, D00I05. https://doi.org/10.1029/2009JD012388

Oberheide, J., Shiokawa, K., Gurubaran, S., Ward, W. E., Fujiwara, H., Kosch, M. J., et al. (2015). The geospace response to variable inputs from the lower atmosphere: A review of the progress made by Task Group 4 of CAWSES-II. *Progress in Earth and Planetary Science*, *2*(1), 1–31. https://doi.org/10.1186/s40645-014-0031-4

Prolss, G. W. (2011). Density perturbations in the upper atmosphere caused by the dissipation of solar wind energy. *Surveys in Geophysics*, *32*(2), 101–195. https://doi.org/10.1007/s10712-010-9104-0

Prolss, G. W., & Zahn, U. (1977). Seasonal-variations in latitudinal structure of atmospheric disturbances. *Journal of Geophysical Research*, *82*(35), 5629–5632. https://doi.org/10.1029/JA082i035p05629

Qian, L., Burns, A. G., Emery, B. A., Foster, B., Lu, G., Maute, A., et al. (2014). The NCAR TIE-GCM: A community model of the coupled thermosphere/ionosphere system. In J. Huba, R. Schunk, & G. Khazanov (Eds.), *Modeling the Ionosphere-Thermosphere System*, American Geophysical Monograph (pp. 73–84). Washington: John Wiley & Sons. https://doi.org/10.1029/2012GM001297

Qian, L., Burns, A. G., Wang, W., Solomon, S. C., & Zhang, Y. (2016). Longitudinal variations of thermospheric composition at the solstices. *Journal of Geophysical Research: Space Physics*, *121*(7), 6818–6829. https://doi.org/10.1002/2016JA022898

Richmond, A. D., & Lu, G. (2000). Upper-atmospheric effects of magnetic storms: A brief tutorial. *Journal of Atmospheric and Solar-Terrestrial Physics*, *62*(12), 1115–1127. https://doi.org/10.1016/s1364-6826(00)00094-8

Richmond, A. D., Ridley, E. C., & Roble, R. G. (1992). A thermosphere/ionosphere general-circulation model with coupled electrodynamics. *Geophysical Research Letters*, *19*(6), 601–604.

Roble, R. G. (1983). Dynamics of the Earth's thermosphere. *Reviews of Geophysics*, *21*(2), 217–233. https://doi.org/10.1029/RG021i002p00217

Roble, R. G., & Ridley, E. C. (1987). An auroral model for the NCAR thermospheric general circulation model (TGCM). *Annales de Geophysique*, *5A*(6), 369.

Roble, R. G., Ridley, E. C., Richmond, A. D., & Dickinson, R. E. (1988). A coupled thermosphere ionosphere general-circulation model. *Geophysical Research Letters*, *15*(12), 1325–1328.

Sarris, T. E. (2019). Understanding the ionosphere thermosphere response to solar and magnetospheric drivers: Status, challenges and open issues. *Philosophical Transactions of the Royal Society a-Mathematical Physical and Engineering Sciences*, *377*(2148). https://doi.org/10.1098/rsta.2018.0101

Solomon, S. C. (2017). Global modeling of thermospheric airglow in the far ultraviolet. *Journal of Geophysical Research: Space Physics*, *122*(7), 7834–7848. https://doi.org/10.1002/2017JA024314

Sutton, E. K., Forbes, J. M., & Nerem, R. S. (2005). Global thermospheric neutral density and wind response to the severe 2003 geomagnetic storms from CHAMP accelerometer data. *Journal of Geophysical Research*, *110*, A09S40. https://doi.org/10.1029/2004JA010985

Vincent, R. A. (2015). The dynamics of the mesosphere and lower thermosphere: A brief review. *Progress in Earth and Planetary Science*, *2*(1), 1–13. https://doi.org/10.1186/s40645-015-0035-8

Ward, W. E. (1999). A simple model of diurnal variations in the mesospheric oxygen nightglow. *Geophysical Research Letters*, *26*(23), 3565–3568. https://doi.org/10.1029/1999GL003661

Yue, J., & Wang, W. B. (2014). Changes of thermospheric composition and ionospheric density caused by quasi 2 day wave dissipation. *Journal of Geophysical Research: Space Physics*, *119*(3), 2069–2078. https://doi.org/10.1002/2013JA019725